To appear as a chapter in Blast Mitigation: Experimental and Numerical Studies, Editors A. Shukla, Y. Rajapakse, and M.E. Hynes, Springer, in press 2013.

Dynamic Buckling and Fluid-Structure Interaction of Submerged Tubular Structures

Neal P. Bitter and Joseph E. Shepherd

Abstract Dynamic buckling of submerged structures is a challenging problem for which experimental data is scarce and generalized theoretical models are difficult to employ. In addition to the complexities of dynamic buckling, this problem features additional difficulties due to the strong fluid-solid interaction that is characteristic of structures submerged in a dense fluid. This chapter reviews some recent experiments in which time-resolved measurements of pressure and strain were made during the buckling of submerged tubes. This data clarifies the buckling behavior over a useful range of conditions and provides a means to validate theoretical models with a rigor not possible using post-collapse measurements alone. Observations from the experiments are then used to develop simple models of buckling and fluid-structure interaction; comparisons with the experimental data demonstrate good agreement in spite of the many simplifications used in the modeling.

1 Introduction

Designing submerged structures to withstand blast loads is a challenge encountered in numerous military and industrial applications. The fundamental difference between blast loads in a gaseous medium and blast loads in a dense fluid, like water, is the strength of the coupling between the fluid and solid motion. This strong coupling complicates dynamic failure predictions since the fluid and solid motion cannot in general be solved independently. The presence of a dense fluid can play an important role in the failure of the structure. For instance, structural deformation can produce local volume changes in the fluid domain which reduce the intensity of the pressure

Neal P. Bitter
California Institute of Technology, Pasadena, CA USA 91125 e-mail: nbitter@caltech.edu

Joseph E. Shepherd
California Institute of Technology, Pasadena, CA USA 91125 e-mail: joseph.e.shepherd@caltech.edu

load. In addition, the added mass of the fluid can alter the timescales of structural motion, and radiation of energy into the surrounding fluid provides an additional damping mechanism not present for freely-vibrating structures. To address these complications, the effects of fluid-structure interaction (FSI) are carefully considered as we study dynamic buckling in this chapter.

One of the most common and detrimental failure modes of submerged structures is buckling of hollow components due to external pressure. Components of cylindrical shape are frequently used in marine applications, and this shape is also a useful idealization of more complicated real geometries. Accordingly, this chapter considers dynamic buckling in the specific context of cylindrical tubes, focusing in particular on tubes loaded by axisymmetric shock waves which travel along the tube axis. More general load cases, such as a blast wave impinging on the side of the tube or at an angle relative to the tube axis, are beyond the scope of this review, but some experimental data (Lindberg and Sliter, 1969) are available for the case of blast waves in air. For experimental convenience, we also do not consider the effects of uniform hydrostatic pressure, assuming instead that the magnitude of the blast load is much greater than the hydrostatic component of pressure. However, the theoretical models presented here are easily extended to include hydrostatic effects that are encountered in practice.

Static buckling of cylindrical tubes due to external pressure has been studied for several decades, and classical theories such as the linear theory of Timoshenko and Gere (1961) provide reasonable estimates of the buckling threshold under many conditions; the accuracy of these predictions is especially good for long tubes (Batdorf, 1947). Much effort has also been committed towards modeling the effects of boundary conditions (Sobel, 1964, Galletly and Bart, 1956), shape imperfections (Hutchinson and Koiter, 1970, Kempner et al., 1957, Koiter, 1945), and non-linear pre-buckling deformation (Yamaki, 1969, Stein, 1964), and considerable progress has been made. Review papers on static buckling have been written by Simitses (1986) and Teng (1996), and a detailed description of the most common theoretical techniques for elastic static buckling is given by Yamaki (1984).

For transient pressure loads, the analysis is in some ways more complicated. Due to inertial effects, structures can usually withstand loads significantly exceeding the static buckling limit, provided that the duration is sufficiently short. As a result, the buckling threshold depends on both the amplitude of the applied load and its duration, or equivalently, its impulse. For time-varying loads, there is also potential for large deformations due to resonance, which may be caused either by periodic forcing or by autoparametric resonance (Goodier and McIvor, 1964, Lindberg, 1974). In this review, such resonance is not considered because our experiments show that the effects of fluid-structure interaction and internal material damping limit the amplitude of axisymmetric vibrations and inhibit autoparametric excitation.

In the 1960s, an extensive research effort was initiated by the Air Force Weapons Laboratory to study dynamic buckling of tubes subjected to blast waves in air (Lindberg et al., 1965, Abrahamson et al., 1966, Lindberg and Firth, 1967, Lindberg and Sliter, 1969, Lindberg and Florence, 1987). These experiments used several different configurations of explosives to measure the dynamic buckling threshold over a

range of pressures and impulses, and fair agreement with two-dimensional, plane-strain models was found.

As an outcome of these experiments, Lindberg (1964) reported on the buckling of very thin shells ($a/h = 480$) subjected to "impulsive loads", that is, loads which have a duration much less than the response time of the tube. He found that the tube's buckling behavior was controlled purely by elastic effects. Abrahamson et al. (1966) studied the corresponding problem of thick shells ($a/h = 10 - 30$) subjected to impulsive loads, and showed that the response is governed primarily by effects of plasticity. Anderson and Lindberg (1968) investigated the response of tubes under "quasi-impulsive" loads, i.e., loads having a duration comparable to the response time of the tube. They found that both elastic and plastic effects can be important and developed a model which takes this factor into account.

A common challenge in all of these studies was making a direct comparison between experiments and theoretical models. In many of the experiments, the response was evaluated only through post-collapse analysis, so the predictions of models during the intermediate stages of buckling could not be evaluated. In a few instances (Lindberg, 1974, Lindberg et al., 1965) dynamic strain measurements were recorded; however, only limited data was reported and the strain traces exhibited many features which could not be easily explained by the theoretical models.

Recently we have developed an experimental facility for studying buckling of submerged tubes in which the loads are applied using shock waves in water rather than blast waves in air. This approach enables dynamic strain measurements to be made while the tube buckles, which provides significantly more information about the mechanics of failure than can be obtained from post-collapse inspection alone. In addition, our experimental facility can operate in regions in the parameter space that are not easily reachable using explosives, and can also explore the effects a dense fluid surrounding the tube. As a result, our new experiments nicely complement previous results and allow for a more thorough evaluation of theoretical dynamic buckling models.

The first part of this chapter presents some recent experimental measurements of the buckling behavior of submerged tubes. The specimen tubes are relatively thick, with ratios of radius to wall thickness in the range of 13-25. The duration of the applied pressure load is 50-100 times the period of axisymmetric vibration, so the response is considered "quasi-static". However, the peak pressures required to buckle the tubes are still 5-10 times greater than the static buckling pressure, demonstrating the importance of inertial effects. For the load conditions considered in this chapter, the buckling behavior is controlled by elastic effects alone.

The second part of this chapter describes an approximate theoretical model of the tube's buckling behavior. Observations from experiments are used to justify several simplifications, including the treatment of the tube as a 2D ring in a state of plane strain along its axis. This model is then used to predict the dynamic response of tubes and generate buckling threshold curves, and good agreement with experimental data is found in both cases.

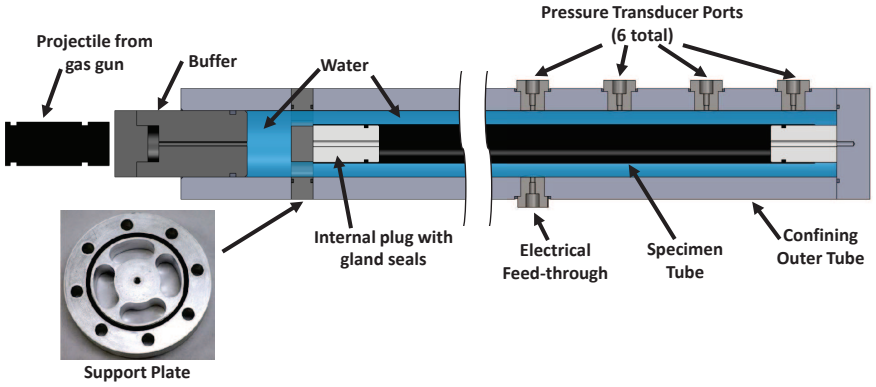

Fig. 1 Diagram of experimental apparatus. Confining outer tube is 1.1 m long overall and 127 mm in outer diameter. Inset: photograph of support plate (127 mm outer diameter) used to prevent axial loading of the specimen tube.

2 Experimental Results

Figure 1 shows a diagram of our experimental facility, which is an adaptation of the apparatus developed by Damazo et al. (2010). A thin-walled specimen tube is mounted concentrically inside of a larger cylindrical vessel made of 4140 high strength steel and having an inner radius of 38.1 mm and wall thickness of 25.4 mm. The ends of the specimen tube are supported and sealed using internal plugs with gland seals. These plugs restrict inward radial motion of the specimen tube, but do not constrain axial displacement except through the friction between the tube and plug that is generated as the tube compresses. The upper plug (left side of Fig. 1) is fixed to a support plate so that pressure waves in the water do not produce an axial load on the specimen tube. As shown in the inset photograph, this support plate features four holes which allow pressure waves to pass through.

The annular space between the specimen tube and the thick-walled outer tube is filled with water, and a small volume of water is also present above the support plate. Shock waves in the water are generated using a vertical gas gun, which is described in more detail by Inaba and Shepherd (2010). The gas gun fires a steel projectile into a buffer, which generates a stress wave that is then transmitted into the water and travels along the outside of the specimen tube. The resulting pressure pulse in the water is approximately exponential in shape, and the rate of decay is dictated by the wave mechanics in the projectile and the buffer. As a result, the duration of the pressure pulse and can be controlled by changing the lengths and materials of these two components. The results reported in this chapter were obtained using a 1.5 kg steel projectile that is 120 mm long and 50 mm in diameter. The buffer is made from either aluminum or steel and is 130 mm long. The buffer is capped with a 25.4 mm thick steel striker plate to prevent damage during the projectile impact.

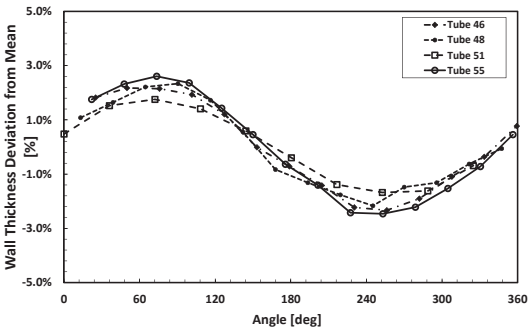

a)

b)

Fig. 2 a) Variations in wall thickness around the circumference of several specimen tubes. Variations are reported as a percentage of the mean wall thickness. b) Photograph of a tube buckled in mode 2 orientation. Tube is 6061-T6 aluminum with $a = 15$ mm and $a/h = 17.4$.

The characteristics of the pressure wave, such as speed, peak pressure, and impulse, are measured using a row of six piezo-electric pressure transducers (PCB model 113A23) along the side of the thick-walled outer cylinder. The transducers have a response time of less than 1 μs and a resonant frequency greater than 500 kHz, and are sampled at 1 MHz. Since the radii of the specimen tube and the outer cylinder differ by only 15-20 mm, the radial transit time of pressure waves through the annulus of water is about 10-15 μs, which is quite short compared to the other timescales involved in the problem. As a result, the measured pressure is expected to be very close to that at the surface of the specimen tube.

Deformation of the specimen tube is measured using bonded strain gauges, which are coated with a compliant sealant (Vishay PG, M-Coat D) to eliminate electrical interference by the water. Signals are amplified using a Vishay 2310B signal conditioners operated in wide-band mode (-3 dB at 250 kHz) and digitized at 1 MHz. The strain gauges are usually installed in the hoop direction, and by installing multiple gauges around the circumference of the tube at a given axial location, the number of lobes (usually 2-3) in which the tube vibrates or buckles can be determined.

The specimen tubes are all 0.91 m long and have radii a of 15, 20, or 22 mm and wall thicknesses h of 0.9, 1.25, or 1.5 mm. The combinations of radius and wall thickness that were tested give a/h in the range 13-25 and L/a in the range of 40-60. Tubes were made from 6061-T6 aluminum, 3003-H14 aluminum, or 304 stainless steel. The steel tubes were of welded construction, while the aluminum tubes were extruded (seamless).

We have found that systematic variations in wall thickness of the specimen tubes significantly affect the orientation of the buckles. For extruded tubes, the wall thickness typically varies sinusoidally around the circumference, as depicted in Fig. 2a where measurements were made using a round-tipped micrometer. These variations in wall thickness appear to be uniform or slowly-varying along the axis of the tube.

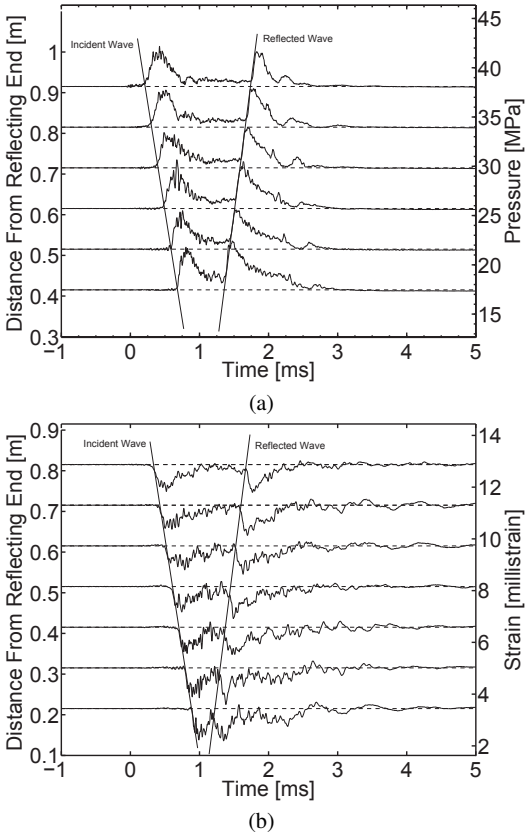

Fig. 3 Pressure (a) and strain (b) histories for a tube with $p_{max}/p_{static} = 1.4$. Tube is 6061-T6 aluminum with radius a = 15 mm and a/h = 17.4.

It is important to point out that other types of imperfections, such as non-circular shape or residual stresses, may also be present. However, as shown in Fig. 2b, our experiments indicate that variations in wall thickness are the dominant imperfection since the major axis of mode 2 buckles always aligns with the point of minimum wall thickness. This consistent behavior also facilitates dynamic strain measurements: the strain gauges can be placed along the thinnest side of the tube to measure the maximum strains that occur.

2.1 Linear Elastic Deformation

For pressure waves of small enough amplitude or short enough duration, the tube's response is elastic and primarily axisymmetric. Examples of pressure and strain

traces, plotted on an x-t diagram, are shown in Fig. 3. An incident wave characterized by a jump in pressure followed by an exponential decay travels along the tube with an approximately constant speed and wave profile. This wave then reflects off of the bottom end of the test fixture and traverses the specimen tube once more. Note that the maximum pressure is greater than the static buckling pressure by a factor of 1.4, yet the motion remains axisymmetric. This occurs because the duration of the pressure pulse is short and buckles do not grow rapidly enough at this pressure to be observable.

It is interesting to note that the tube's response for low pressures is analogous to that of a waterhammer event occurring in an internally pressurized tube. Such a situation was examined using a very similar projectile-impact facility by Inaba and Shepherd (2010), who recorded pressure and strain traces that look very much like those in Fig. 3. This suggests that the axisymmetric deformation that occurs prior to buckling can be predicted using models that have been developed and thoroughly evaluated by the waterhammer community (Tijsseling, 1996, Wylie and Streeter, 1993, Wiggert and Tijsseling, 2001, Shepherd and Inaba, 2010).

2.1.1 Simple Model of Pressure Wave

One of the simplest of these waterhammer models, first devised by Korteweg (1878) and experimentally validated by Joukowsky (1900), is based on the assumption that radial inertia of the tube and fluid, as well as the effects of bending of the tube along its axis, are small. These assumptions are strictly valid only for low frequencies and long wavelengths, but experiments by Inaba and Shepherd (2010) have demonstrated that the performance of this model is quite good for many practical conditions. As discussed by Shepherd and Inaba (2010), the speed c_k of the coupled fluid-solid wave predicted by the Korteweg-Joukowsky theory is given by:

$$c_k = \frac{c}{\sqrt{1+\beta_k}} \tag{1}$$

where

$$\beta_k = c^2 \rho_w \frac{2a}{Eh}$$

Here β_k is a dimensionless parameter that describes the extent of fluid-solid coupling, which increases as β_k increases. Given the success of this simple model for analyzing pressure waves inside of tubes, this theory will be extended for use in the present annular geometry.

If the width of the fluid annulus is small enough that the radial reverberation time of pressure waves is small compared to other timescales, then it is reasonable to model the fluid pressure as averaged across the annular gap. This is equivalent to neglecting the radial inertia of the fluid. Using this assumption, the linearized equations of conservation of mass and momentum (Lighthill, 1978) of the fluid can

be combined and written in the following form:

$$\frac{\partial^2 p}{\partial x^2} = \frac{1}{c^2}\frac{\partial^2 p}{\partial t^2} + \frac{\rho_w}{A_o}\frac{\partial^2 A'}{\partial t^2} \tag{2}$$

where ρ_w is the fluid density, A_o is the original cross-sectional area of the annulus, and A' is the change in area due to deformation. As this equation shows, the system obeys the usual linear wave equation for the pressure with an additional term involving the change in cross sectional area A of the tube. This additional term models the compliance of the tube wall and, as will be shown, has the effect of reducing the speed of pressure waves.

Deformation of both the inner and outer tubes of the annular channel are modeled. Deflection of the outer tube (radius b) is denoted w_o and is taken positive outward, while deformation of the inner tube (radius a) is denoted w_i and assumed positive inward. The area A of the channel can then be written in terms of these deformations.

$$\begin{aligned} A(x,t) &= A_o + A'(x,t) \\ &= \pi(b^2 - a^2) + 2\pi(aw_i + bw_o) \end{aligned} \tag{3}$$

The Korteweg-Joukowsky hypothesis neglects bending and inertia of the tube, treating it as a massless membrane. Using this approximation, the radial deformations of the inner and outer tubes are proportional to the pressure:

$$w_i = \frac{pa^2}{E_i h_i} \qquad\qquad w_o = \frac{pb^2}{E_o h_o} \tag{4}$$

where E and h are the elastic modulus and wall thickness. Substituting (3) and (4) into (2) produces a wave equation with a modified wave speed:

$$\frac{\partial^2 p}{\partial x^2} = \left[\frac{1}{c^2} + \frac{2\rho_w}{b^2 - a^2}\left(\frac{a^3}{E_i h_i} + \frac{b^3}{E_o h_o}\right)\right]\frac{\partial^2 p}{\partial t^2} \tag{5}$$

The effective wave speed can be expressed in the form of (1) if a modified fluid-solid coupling parameter β_{mod} is used:

$$\beta_{mod} = \frac{2\rho_w c^2}{b^2 - a^2}\left(\frac{a^3}{E_i h_i} + \frac{b^3}{E_o h_o}\right) \tag{6}$$

The predictions of this theory are compared with our present experimental measurements in Fig. 4. The experimental wave speeds were obtained made by fitting a line to time-of-arrival data from the pressure measurements and computing the slope of this line. In all cases, the experimentally measured wave speeds are within 1-4% of the theoretical predictions; the fact that the experimental speeds are consistently low is likely due to air bubbles in the water which accumulate when the vessel is filled.

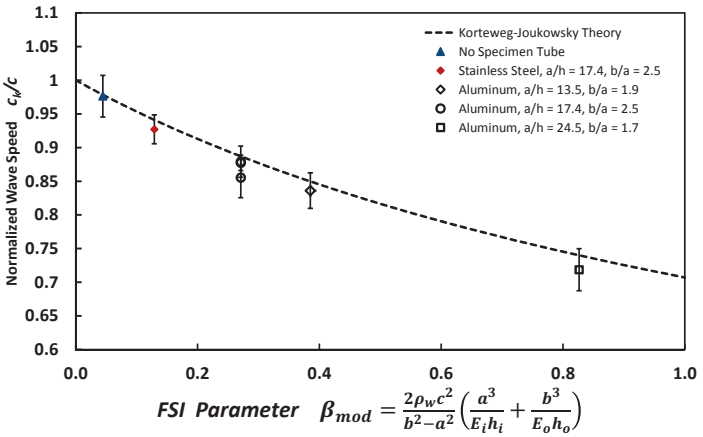

Fig. 4 Comparison of predicted and measured wave speeds for several tube materials and sizes.

2.1.2 Coupling between Fluid and Solid Motion

The high frequency oscillations observed in the pressure and strain traces of Fig. 3 are not unidentifiable "noise", but rather are repeatable axisymmetric vibrations that are excited by the sharp pressure wavefront. This fact is shown more clearly for a different tube in Fig. 5, where pressure and strain traces at a single axial location are directly compared with one another. At this axial location, three hoop strain gauges have been installed: one is mounted on the thinnest side of the tube, while the other two are offset by 90° and 180° around the circumference. The phase difference between these gauges then indicates whether or not the motion is axisymmetric. Upon arrival of the incident pressure wave at $t = 0$, the tube begins to vibrate axisymmetrically, as indicated by the close agreement of all the strain gauges. At about t = 0.5 ms, the reflected pressure wave from the bottom of the tube arrives and further increases the pressure and strain. At this point a slight departure from axisymmetric motion is observed. As the pressure wave dies away, the tube continues to vibrate in a mode 2 shape, as indicated by the fact that strain gauges positioned 180° apart are in phase while gauges 90° apart are out of phase.

Figure 5 leads to several important conclusions about fluid-structure interaction in this geometry. The first observation is that as long as the deformation remains axisymmetric, the pressure is very nearly proportional to the strain. In fact, on the time interval of 0 – 0.5 ms the instantaneous measured strain $\varepsilon(t)$ is within about 10% of the predicted static value based on the instantaneously measured pressure $p(t)$:

$$\varepsilon(t) = \frac{p(t)a(1-\nu^2)}{Eh} \tag{7}$$

This suggests that the effects of bending along the tube axis are small and the use of a membrane-type model for the pre-buckling motion of the tube is reasonable.

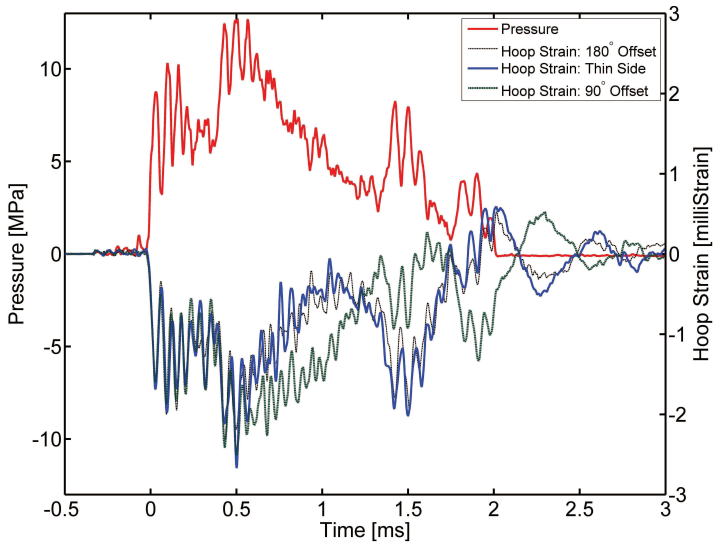

Fig. 5 Comparison of pressure and strain traces 250 mm from the reflecting end wall. Tube is 6061-T6 aluminum with $a = 20$ mm, $a/h = 13.5$, and $p_{max}/p_{static} = 2.5$.

A second important observation is that the amplitude of axisymmetric vibrations is fairly small compared to the quasi-static component of strain, and the vibrations die away on the order of tens of cycles. Furthermore, as the specimen tube is made thinner (such as in Fig. 3), the vibratory component of strain becomes even smaller. This differs from situations in which the effects of FSI are negligible, such as a tube subjected to an internal shock or detonation wave. In those cases, the amplitude of vibration is about twice the quasi-static strain and the vibrations can persist for many cycles without significant change in amplitude (Shepherd, 2009). Based on these observations, it is reasonable to expect that autoparametric excitation due to the interaction between the axisymmetric and non-axisymmetric modes will not be significant in our present experiments.

A third observation from Fig. 5 is that unlike the axisymmetric vibrations, non-axisymmetric vibrations are not strongly coupled to the fluid pressure. This is clearly demonstrated by examining the pressure and strain traces after $t = 2$ ms, where the tube continues to vibrate in a mode 2 shape but the pressure remains constant. This behavior suggests that the non-axisymmetric vibrations are nearly volume-preserving, at least provided that these vibrations are small. The smallness criterion can be estimated by considering an annulus of water of outer radius b and inner radius a, with the inner tube subjected to a radial deformation w in the form of a Fourier series:

$$w(\theta,t) = w_o(t) + \sum_{n=1}^{\infty} w_n(t)\cos(n\theta) \tag{8}$$

If it is assumed that one particular mode $n = N$ is dominant, then the relative change in volume of the annulus due to the deformation (8) is given by:

$$\frac{\Delta V}{V} = \left(\frac{2w_o}{a} + \frac{w_o^2}{a^2} + \frac{w_N^2}{2a^2} \right) / \left(\frac{b^2}{a^2} - 1 \right) \tag{9}$$

Typically $w/a << 1$, so the linear term is dominant and the change in volume depends primarily on the axisymmetric motion. It will be shown in Section 3.2.1 that the non-axisymmetric vibration frequencies are low enough that the radiated pressure field is negligible, which means that changes in pressure scale with the volume change:

$$\Delta p = K_f \frac{\Delta V}{V} \tag{10}$$

where K_f is the bulk modulus of the liquid. As a result, the change in pressure due to non-axisymmetric vibrations alone (i.e., for $w_o = 0$) can be expressed as:

$$\Delta p = \frac{K_f}{2(b^2/a^2 - 1)} \left(\frac{w_N}{a} \right)^2 \tag{11}$$

For a practical situation, such as a steel tube submerged in water and deformation restricted to less than the yield strain, this pressure is less than about 50 kPa unless b/a is very small (less than about 1.05). This result shows that non-axisymmetric deformation has only a small effect on the pressure in the fluid surrounding the tube, and hence the speed and amplitude of pressure waves depend primarily on the axisymmetric component of deformation. This fact will also be demonstrated experimentally in the following sections where experimental results at higher pressures are considered. The implication is that in developing buckling models, the motion of the pressure wave can initially be decoupled from the buckling deformation.

2.2 Nonlinear Elastic Deformation

As we have already observed in Fig. 5, higher pressures begin to excite non-axisymmetric modes of deformation. As the pressure or impulse of the load increases further, these non-axisymmetric motions grow rapidly and become much larger than the axisymmetric component of deformation. An example of this is shown in Fig. 6.

The speed and shape of the pressure wave resemble those shown for lower pressures (e.g., Fig. 3), but the response of the tube is quite different. The strain traces feature a series of large amplitude, mode 2 vibrations which persist for much longer than the duration of the pressure load. Despite the excitation of non-axisymmetric displacement, the motion remains elastic and no permanent deformation is observed.

The three strain gauges located at the bottom of the tube (150 mm from the reflecting end) are spaced 90° apart around the circumference. The two strain gauges on opposing sides of the tube are exactly in phase with one another, while the strain

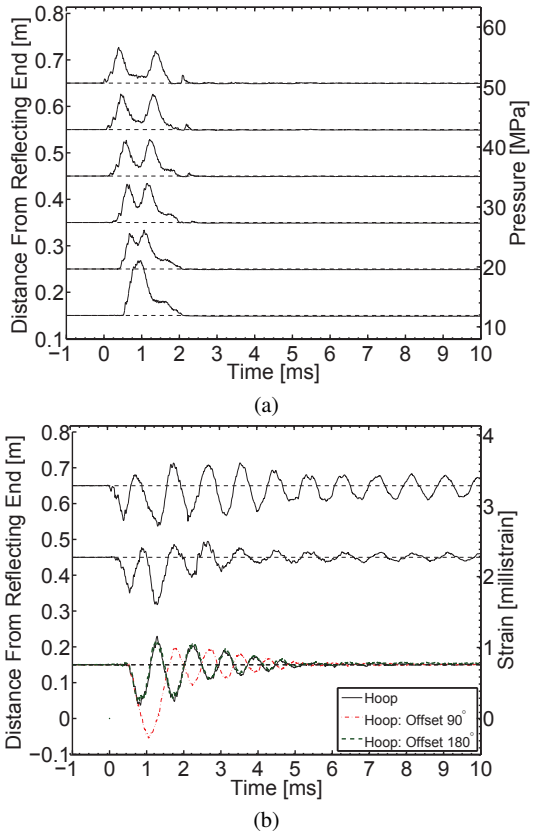

Fig. 6 Pressure (a) and strain (b) histories with multiple strain gauges around the circumference at a single axial location. Tube is 304 stainless steel with radius a = 22 mm and a/h = 18.5. $p_{max}/p_{static} = 1.2$.

gauge between them is exactly out of phase. This confirms that the deformation consists of two lobes. Note that the two gauges on opposite sides of the tube have been attached at the thickest and thinnest points on the tube wall. Thus the major axis of vibration is exactly aligned with the points of maximum and minimum wall thickness, indicating that this imperfection plays a key role in determining the orientation of the vibration.

It is interesting to note that in Fig. 6 the maximum pressure was 1.2 times the static buckling threshold and non-axisymmetric deformation was observed, while in Fig. 3 no non-axisymmetric deformation occurred despite having a larger value of $p_{max}/p_{static} = 1.4$. The reason for this behavior is that the load duration is the same in both cases, but due to differences in material properties (steel vs. aluminum) and tube diameter (22 mm vs 15 mm), the natural frequency of the tube in Fig. 3 is about 1.5 times that of the tube in Fig. 6. Thus when normalized by the tube's

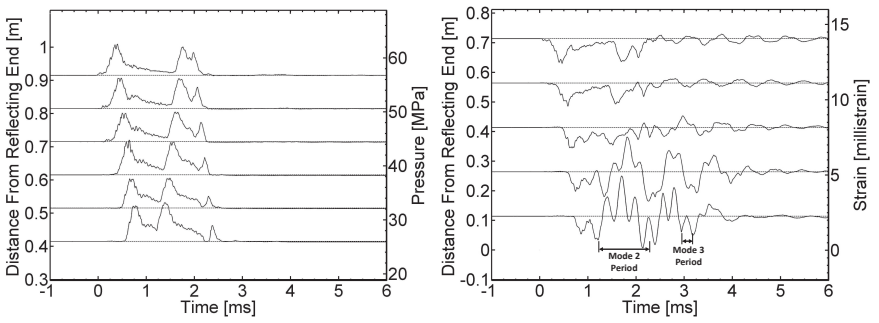

Fig. 7 Pressure (a) and strain (b) traces showing superposed deformation of modes 2 and 3. Tube is 6061 aluminum with radius a = 15 mm and a/h = 17.4. $p_{max}/p_{static} = 2.0$.

response time, the load duration for the tube in Fig. 6 is about 1.5 times longer and hence non-axisymmetric deformation is more strongly excited.

For thinner tubes and higher pressures, vibration in mode numbers greater than 2 can be observed. An example of mode 3 vibrations is shown in Fig. 7. The strain traces exhibit a superposition of vibrations in mode 2 (longer period of about 1 ms) and mode 3 (shorter period of about 0.3 ms). These vibration periods agree closely with theoretical predictions (described in more detail in Sec. 3.2.1), which helps confirm that the behavior has been correctly interpreted. This superposition of multiple excited modes is a well-known feature of dynamic buckling and is more pronounced for shorter impulses and thinner tubes (Lindberg, 1974, Lindberg and Florence, 1987). Note that the mode 3 vibrations are excited only near the reflecting end of the tube where the pressure is greatest; elsewhere the pressure is insufficient to destabilize these modes and only mode 2 vibrations are (slightly) excited.

In many of these experiments, axial strains have also been measured in order to determine whether or not bending along the tube axis plays in important role in the buckle development. The data has revealed that axial bending is negligible, since the measured axial strains are almost exclusively caused by Poisson coupling with the hoop strain. This is demonstrated in Fig. 8 where the measured axial strain ε_x is compared with the axial strain due to Poisson coupling: $-\nu\varepsilon_\theta$. The only place where these two quantities differ substantially is in the precursor wave, which is to be expected since the precursor wave is a longitudinally dominant wave (Shepherd and Inaba, 2010). Over the rest of the trace, the agreement is quite good, which indicates that the effects of bending along the tube axis (which would otherwise show up prominently in the axial strains) are quite small. This result adds further support for the use of a membrane-type model to predict the tube motion prior to buckling.

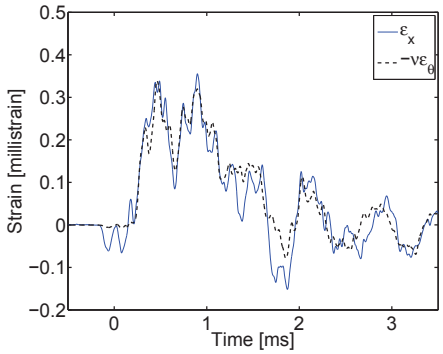

Fig. 8 Comparison of hoop (ε_θ) and axial (ε_x) strains 250 mm from the reflecting end of the tube. Gauges are spaced 90°apart circumferentially. Tube is 3003-H14 aluminum with a = 15 mm, a/h = 17.4, and p_{max}/p_{static} = 1.8.

2.3 Onset of Plastic Deformation

Further increases in the load's pressure or duration lead to plastic deformation and the formation of plastic hinges at the extremities of the buckle where the strain is the greatest. This behavior is demonstrated in Fig. 9, where pressure and strain traces are plotted for three consecutive shots using the same tube from shot to shot.

The first shot, marked (1), produced purely elastic deformation with a peak strain of 4.2 millistrain (which is very close to the yield strain of about 4.5 millistrain for 6061 aluminum); the pressure and strain traces in this shot look very similar to those shown in previous elastic cases (for example, Fig. 6).

The second shot, marked (2), has a peak strain of 6.3 millistrain, which exceeds the yield strain. As a result, slight permanent deformation is observed as indicated by the final strain offset of about 0.9 millistrain due to the residual stresses. Note that the pressure trace in this shot looks very similar to that of the preceding shot, which again supports the conclusion that the pressure wave is unaffected by the non-symmetric elastic vibration, even for relatively large strains.

In the third shot, marked (3), the peak strain is 7.7 millistrain and additional permanent deformation is observed. The strain is no longer oscillatory since much of the kinetic energy is dissipated via plastic work. In this case, the pressure trace looks quite different from that of the preceding shot. Despite a 5% increase in projectile velocity from the gas gun, the peak pressure dropped by about 40% relative to the preceding shot. Furthermore, the pressure wave spreads out and decays more slowly over time. This dispersion of the pressure wave and reduction in peak pressure are likely caused by the residual plastic deformation from the preceding shot. Evidently plastic deformation is not volume preserving, so pressure waves disperse as they encounter the volume change in regions of plastic deformation. This result suggests that the our prior conclusion that the pressure wave can initially be decoupled from non-axisymmetric motion is only valid until plastic deformation occurs.

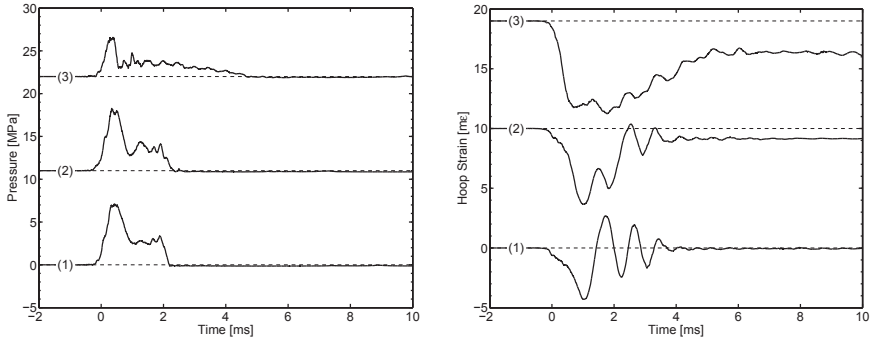

(a) (b)

Fig. 9 Comparison of pressure (a) and strain (b) traces for three consecutive shots. For clarity, the traces have been offset vertically from one another. Traces are recorded 0.25 m from the reflecting end. Tube is 6061-T6 aluminum with $a = 15$ mm and $a/h = 17.4$.

2.4 Single-Shot Collapse

The final regime of motion considered in these experiments is single-shot collapse, which occurs when the pressure and impulse are high enough to catastrophically fail the tube during a single pressure pulse. Examples of pressure and strain traces for a collapsing tube are shown in Fig. 10. Unlike the results shown previously, in which pressure and strain were measured near the bottom end of the tube where the pressure is greatest, in this shot the pressure and strain were measured 150 mm from the top end of the tube. For high pressure shots, this is the location at which collapse first occurs.

The strain trace exhibits a series of vibrations superimposed over an offset that steadily increases with time. The frequency these vibrations is the same as those shown in Fig. 7, which indicates that these are mode 3 vibrations. The permanent deformation observed after the test, shown in Fig. 11, was also mode 3, which supports this interpretation. The increasing offset of this strain trace appears to be the plastic component of strain. The fact that the peak-to-peak amplitude of the vibrations is equal to twice the yield strain lends further support for this conclusion. An interesting observation is that the buckle grows on a timescale that is significantly slower than that of the pressure wavefront. As a result, the leading edge of the pressure wave is not affected by the buckle. However, the pressure drops off sharply behind the incident wave, and the reflected pressure wave at about 1.2 ms is substantially attenuated.

It is interesting to consider whether the permanent deformation observed in these results is associated with flexure due to buckling alone, or consists also of hoop yielding. For loads with duration longer than the period of axisymmetric vibration, the pressure p_y beyond which the tube is brought to hoop yield is given by:

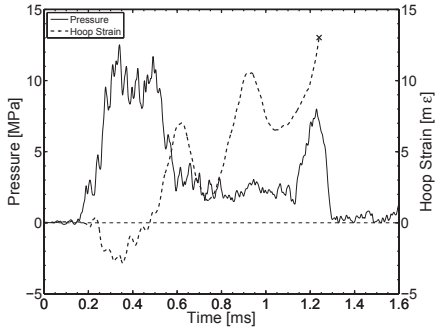

Fig. 10 Pressure and strain traces for a collapsing aluminum tube of radius a = 15 mm and a/h = 17.4. The static buckling pressure for this tube is 3.7 MPa. Pressure and strain were measured 150 mm from the top end of the tube. The strain gauge de-bonded from the surface of the tube at the point marked by an **x**.

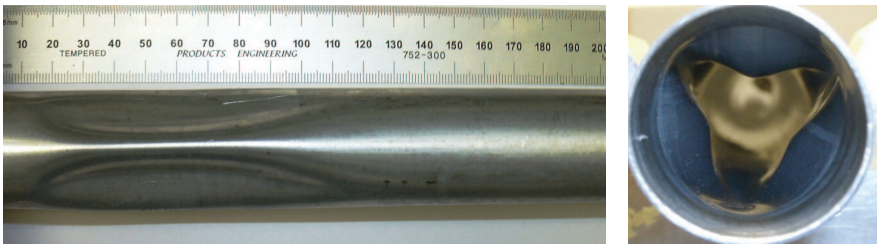

Fig. 11 Post-collapse photographs of tube following the test which generated the data shown in Fig. 10 and illustrating buckling in mode 3. Tube is 6061-T6 aluminum with mean radius a = 15 mm and a/h = 17.4.

$$p_y < \frac{\sigma_y h}{a} \tag{12}$$

where σ_y is the yield stress. For the conditions used in Fig. 10, the pressure limit for hoop yielding is $p_y \sim 17$ MPa. The measured pressure is well below this value, and the overshoot of axisymmetric vibrations due to dynamic loading appears to be small, hence the plastic deformation observed in the strain traces is due primarily to flexure due to buckling.

The data in Fig. 10 are just one example of the possible types of behavior that can occur at higher pressures. As shown in the strain traces, the effects of plasticity become important almost immediately, so the development of the buckle is dictated by both elastic and plastic effects rather than elastic effects alone. An additional difficulty is that as the applied pressure increases, the mode number of the buckles increases and their length decreases. As a result, the buckles become more spatially localized and it is more difficult to measure their development using bonded strain gauges. Interpretation of the resulting strain measurements is also more challenging. Characterizing the buckling behavior under high pressures is a subject of ongoing

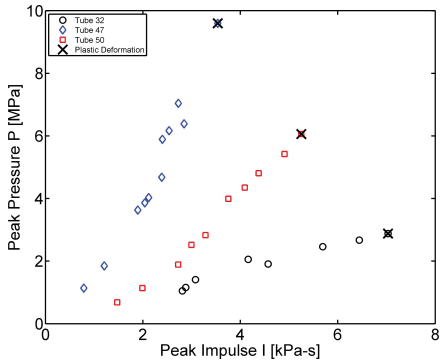

Fig. 12 Pressure vs. impulse curves for three identical tubes under loads of various ratios P/I. Tubes are 6061-T6 aluminum with mean radius a = 22 mm and $a/h = 24.5$. The classical static buckling pressure for these tubes is 1.3 MPa. The bottom curve was generated using an alternate apparatus which features windows for visualization of the buckling process; the compliance of these windows facilitated the small slope P/I achieved in that data set.

investigation in our laboratory, but in this chapter we focus on the behavior at lower pressures and higher impulses where elastic effects are dominant.

2.5 Measurements of the buckling threshold

A convenient experimental criterion for the buckling threshold is the onset of plastic deformation. This criterion is practically meaningful since the tube's strength is greatly reduced after plastic deformation occurs, and this metric can also be applied quite repeatably in experiment using bonded strain gauges. Even if a strain gauge is not located at the point of peak strain, any plastic deformation that occurs produces residual stresses and strains which are readily detected.

For dynamic loads, the buckling threshold is a function of both peak pressure and impulse (Lindberg and Florence, 1987). In principle, then, one could measure the buckling threshold by fixing one of these variables and gradually increasing the other until plastic deformation occurs, which would reveal a single point along the buckling threshold. By repeating this process, one could then map out the buckling threshold over some range of pressures and impulses.

In our experiments, we cannot vary the pressure and impulse independently; rather, the load duration is approximately fixed and as the speed of the projectile from the gas gun increases, the pressure and impulse increase in proportion to one another with the load duration as the constant of proportionality. The load duration is governed by the wave dynamics between the buffer and projectile used to generate the pressure pulse (see Fig. 1), so adjustment of the pulse duration is accomplished by changing the materials and dimensions of these components. Our measurements

of the buckling threshold are then made by fixing the load duration and increasing the pressure and impulse until plastic deformation occurs.

An example of the measured buckling threshold for three identical tubes is shown in Fig. 12. Each line of data points represents a sequence of consecutive shots for which the peak pressure and impulse were gradually increased, and the slopes of these lines were adjusted by changing the duration of the load. The dark **x**'s mark the points at which plastic deformation first occurred, and hence they map out a segment of the buckling threshold.

This data exhibits the expected trend that the tube is able to withstand greater pressures when the impulse is shorter. The classical static buckling threshold for this tube is 1.3 MPa, so pressures more than seven times this value were needed to fail the tube at the lower impulses. This demonstrates that despite the classification of the load as "quasi-static," effects of inertia are still quite important.

As described by Lindberg and Florence (1987), for very large impulses the buckling threshold curve tends asymptotically towards a horizontal limit that is close to the static buckling pressure. For very short impulses, the threshold curve approaches a vertical limit at a particular critical impulse. However, as the impulse of the load is decreased, the effects of plasticity eventually become important in determining the initial buckling behavior (Abrahamson et al., 1966). We have not yet made measurements in this regime, but some data is available from Lindberg and Sliter (1969) which supports these expectations.

3 Theoretical Models

3.1 Background

The general theory of dynamic buckling due to pressure loads that vary along the tube axis remains rather undeveloped. A few researchers have considered this and related problems and made some progress, but usually the results are restricted to very specific situations or are not readily applied to engineering problems. Instead, progress has been made by applying simplifications that are valid for restricted sets of load conditions or tube geometries. Here we briefly review several noteworthy investigations in order of increasing level of approximation.

To the authors' knowledge, only one researcher has reported on the buckling of cylindrical shells due to transient external pressure loads that are not uniform along the tube axis. Hegemier (1966, 1967) analyzed a class of steady-state traveling loads and demonstrated a reduction in the buckling pressure as the speed of the load increased. He also postulated the existence of a critical load speed at which, in the absence of damping, the tube buckles under arbitrarily low pressures. At this critical speed, the group, phase, and load velocities are all equal, so energy introduced by the load cannot disperse away from the load front. Such behavior is quite similar to the resonance that occurs in tubes loaded internally by shock or detonation

waves, which results in large displacements when the speed of the shock or detonation reaches the same critical velocity (Beltman and Shepherd, 2002, Tang, 1965, Simkins et al., 1993, Schiffner and Steele, 1971).

Several researchers have employed a considerable simplification by assuming that the pressure load is spatially uniform, but still modeling axially-varying pre-buckling displacements. Thus the boundary conditions are strictly enforced at the ends of the tube and the effects of bending along the tube are explicitly modeled. Lockhart and Amigazo (1975) assumed that uniform pressure was instantaneously applied to the tube and held constant for all subsequent time. They obtained the interesting result that in the limit of small imperfections, the dynamic buckling threshold could be obtained directly from the classical buckling load (i.e., for a perfect tube) and the static buckling load (i.e., for an imperfect tube). However, their result is only applicable for loads that are a step function in time and does not apply to finite-duration loads. Their approach is similar to that of Budiansky and Hutchinson, who developed approximate relationships between the dynamic and static buckling loads for general structures rather than for a specific geometry (Budiansky and Hutchinson, 1965, Hutchinson and Budiansky, 1966).

The same problem of a tube subjected to uniform pressure, incorporating axially-varying pre-buckling displacements, was studied by McIvor and Lovell (1968) using Fourier series in both the axial and circumferential directions. This produces a set of ordinary differential equations for the Fourier modes which, due to the nonlinearity of the shell equations, are highly coupled. However, for small deformations, many of the nonlinear terms were found to be negligible and the initial buckling behavior was shown to be governed by a Mathieu-type equation for each Fourier mode. The stability characteristics of this type of equation are quite well-known (McLachlan, 1964).

Due to the difficulty of the general theory of dynamic buckling, most researchers have simplified their analysis to the case of a two dimensional ring. Goodier and McIvor (1964) wrote a landmark paper on the elastic stability of thin shells using this assumption, and Abrahamson and Goodier (1962) developed the corresponding theory for plasticity-dominated motions which occur for thick tubes or very low impulses. The intermediate range in which both elastic and plastic effects are important was considered by Anderson and Lindberg (1968).

The objective of this chapter is not to discuss the general theory of dynamic buckling, but rather to describe some simple theories which still provide useful predictions that agree well with experimental results. Such simple theories also give insight regarding the parameters that affect buckling. In accordance with this goal, a theory that is very similar to that of Goodier and McIvor (1964) is adopted in which the tube is treated as a plane-strain ring. This model is then modified to allow the tube to be loaded by an external pressure rather than an initial radial velocity, as well as to account for the effects of fluid-structure interaction.

3.2 Elastic Two-Dimensional Model

The tube is modeled as a ring in a state of plane strain along the tube axis. This 2D approximation and the model that follows are only valid if several constraints on the geometry and load conditions are satisfied:

Load Speed: In order to apply the 2D approximation, axial motion of the tube and bending along the tube axis must be negligible. This places restrictions on the speed of the applied load. Mann-Nachbar (1962) performed a parameter study which suggests that if a shock wave traveling along a tube moves sufficiently rapidly, then bending stresses are very small and the deformation can be predicted quite accurately using a membrane-type model, which would be equivalent to the present 2D ring. For the membrane model to be accurate, the load must travel faster than the "critical velocity" studied by Beltman and Shepherd (2002). For loads which travel at speeds very close to this critical speed, the displacements and stresses are highly amplified, but as the load speed is raised above the critical velocity, the contribution of axial bending to the total response of the tube decreases rapidly. To a good approximation, this critical speed υ_{cr} can be estimated by (Jones and Bhuta, 1964):

$$\upsilon_{cr} = \left[\frac{E^2 h^2}{3\rho^2(1-\nu^2)^2 a^2}\right]^{1/4} \tag{13}$$

A second constraint is that the load speed must remain below the shear wave velocity $\upsilon_s = \sqrt{\kappa G/\rho}$ and the dilatational wave velocity $\upsilon_d = \sqrt{E/\rho(1-\nu^2)}$; if these conditions are not met then the effects of transverse shear deformation and rotary inertia become important and the membrane-type model is no longer valid (Lin and Morgan, 1956, Chonan, 1977, Naghdi and Cooper, 1956). Fortunately, for metal tubes of practical sizes, the lower limit on the load speed given by (13) is on the order of 500-1000 m/s and the shear wave speed is on the order of 3000 m/s. Many realistic load cases, such as shock waves in water or detonations in gaseous media, travel at velocities which fall between these bounds. For instance, in the present experiment the critical velocity is about 900 m/s, the shear wave speed is about 2800 m/s, and the measured pressure wave speeds are 1200-1500 m/s.

The restriction that the load speed fall between υ_{co} and υ_s provides a general guideline regarding the applicability of membrane-type models. To ensure that the membrane model is sufficiently accurate under a specific set of conditions, one can always solve the axisymmetric problem using a shell theory which includes effects of bending, shear deformation, and rotary inertia (such as the theory of Tang, 1965) and compare the results with the predictions of a membrane model.

Tube Length: The 2D approximation also requires that the length of the specimen tube be much greater than its diameter, so that the local reinforcement due to boundary conditions at the ends of the tube is negligible. In the present experiments, the length of the tube is 0.91 m and the tube radius is $15-20$ mm, so this condition is satisfied.

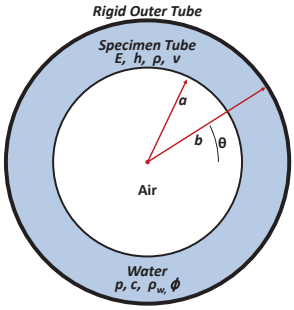

Fig. 13 Diagram of two dimensional ring with surrounding annulus of fluid.

Wavelength of Pressure Wave: In the sections that follow, fluid-structure interaction is analyzed using a 2D fluid model, which is only valid if the axial wavelengths of the pressure load is much greater than the width of the annular gap between the specimen tube and the rigid outer tube. In the present experiments, the spatial extent of the load (duration times speed) is on the order of 1-2 m and the width of the fluid annulus is at most 23 mm, so this criterion is met.

Magnitude of Pressure Pulse: A final restriction on the pressure load is that the maximum pressure must not bring the tube to hoop yield. The maximum pressure which satisfies this condition can be estimated using (12). Abrahamson et al. (1966) have developed a shell theory which is appropriate if this criterion is violated, but since the focus of this chapter is on elastic effects and the corresponding experiments do not involve hoop yield, such a model is not pursued here.

A diagram of the 2D tube model is shown in Fig. 13. The deformable tube under consideration has a radius a, density ρ, elastic modulus E, and Poisson's ratio ν. It is surrounded by an annulus of dense fluid of sound speed c, pressure p, and density ρ_w, which is contained in a rigid outer cylinder of radius b. Radial deformation of the specimen tube is denoted w and is taken positive inward.

The equations of motion that follow are based on a model that was first introduced by Goodier and McIvor (1964) and later described in more detail in the monograph by Lindberg and Florence (1987). In those references, the buckling model was developed for impulsive loads which were represented by applying an initial inward radial velocity to the surface of the tube. In what follows, this model is suitably adapted to allow pressure loads to be simulated and the effects of FSI included. For conciseness, some of the details are omitted when they have been discussed elsewhere; a more comprehensive discussion of these details is available in the previously mentioned references.

For a ring in a state of plane strain, the total hoop strain ε_θ consists of a component due to stretching of the middle surface and a component due to bending:

$$\varepsilon_\theta = \varepsilon_o + \kappa z \tag{14}$$

Here $\varepsilon_o(\theta)$ is the hoop strain at the middle surface of the tube, $\kappa(\theta)$ is the curvature, and z is the normal distance from the middle surface. The membrane strain ε_o and curvature κ are modeled by choosing an appropriate set of strain-displacement relations. Many different strain-displacement models have been proposed (Leissa, 1973, Mushtari and Galimov, 1961), but in the present case the following relations, based on the work of Lindberg and Florence (1987), are selected:

$$\varepsilon_0 = \frac{1}{a}\frac{\partial \mathrm{v}}{\partial \theta} - \frac{w}{a} - \frac{w}{a^2}\frac{\partial \mathrm{v}}{\partial \theta} + \frac{1}{2a^2}\left(\frac{\partial w}{\partial \theta}\right)^2 + \frac{1}{a^2}\left(\frac{\partial w}{\partial \theta}\frac{\partial w_i}{\partial \theta} - w_i\frac{\partial \mathrm{v}}{\partial \theta} - w\frac{\partial \mathrm{v}_i}{\partial \theta}\right) \tag{15a}$$

$$\kappa = \frac{1}{a^2}\left(w + \frac{\partial^2 w}{\partial \theta^2}\right) \tag{15b}$$

In these equations, w and v are the radial and circumferential displacements. Displacements with subscript i describe the shape imperfection, that is, the initial deviation of the tube from a circular shape when no external loads are present. Thus (15) models the changes in membrane strain and curvature that are produced when the tube deforms relative to an initially non-circular shape.

Using the above models, the strain energy U and the kinetic energy T_K per unit length of the tube are expressed as:

$$U = \frac{1}{2}\frac{Eha}{(1-\nu^2)}\int_0^{2\pi}\left(\varepsilon_o^2 + \frac{h^2}{12}\kappa^2\right)d\theta \tag{16a}$$

$$T_K = \frac{1}{2}\rho ha\int_0^{2\pi}\left(\frac{\partial w}{\partial t}\right)^2 + \left(\frac{\partial \mathrm{v}}{\partial t}\right)^2 d\theta \tag{16b}$$

To account for loading by the external fluid pressure, the work W_p per unit length done by the pressure as the tube deforms must also be included.

$$W_p = \int_0^{2\pi}(pw)ad\theta \tag{17}$$

This model is much more conveniently described in terms of several dimensionless parameters:

$$\begin{aligned} [W,V,W_i,V_i]^T &= \frac{1}{a}[w,\mathrm{v},w_i,\mathrm{v}_i]^T & \beta^2 &= \frac{h^2}{12a^2} \\ T &= t\sqrt{\frac{E}{\rho(1-\nu^2)a^2}} & P &= \frac{pa(1-\nu^2)}{Eh} \end{aligned} \tag{18}$$

In terms of these dimensionless parameters, the strain energy, kinetic energy, and pressure work are given by:

$$U = \frac{1}{2}\frac{Eha}{(1-\nu^2)}\int_0^{2\pi}\left(\varepsilon_o^2 + \beta^2(\kappa a)^2\right)d\theta \tag{19a}$$

$$T_k = \frac{1}{2}\frac{Eha}{(1-\nu^2)}\int_0^{2\pi}\left(\dot{W}^2 + \dot{V}^2\right)d\theta \tag{19b}$$

$$W_p = \frac{Eha}{(1-\nu^2)}\int_0^{2\pi} PW\,d\theta \tag{19c}$$

where dots above the variables denote differentiation with respect to the dimensionless time T. The deformations, shape imperfections, and pressure can now be expanded using Fourier series:

$$W = W_o(T) + \sum_{n=2}^{\infty} W_n(T)\cos(n\theta) \tag{20a}$$

$$P = P_o(T) + \sum_{n=2}^{\infty} P_n(T)\cos(n\theta) \tag{20b}$$

$$V = \sum_{n=2}^{\infty} V_n(T)\sin(n\theta) \tag{20c}$$

$$\{W_i, V_i\} = \sum_{n=2}^{\infty} \{\delta_n, \alpha_n\}\cos(n\theta) + \{\gamma_n, \beta_n\}\sin(n\theta) \tag{20d}$$

The sine components of the Fourier series for the displacements W and V have been neglected since the frame of reference can always be rotated such that these components are zero. However, both terms in the expansions for the shape imperfections must be retained since there is no reason to expect that they have the same phase angle as the deformations. In addition, the $n = 1$ mode of deformation has been excluded from the summations since it corresponds to a rigid translation of the tube.

Goodier and McIvor (1964) proposed a significant simplification in which the only extensional component of deformation is W_o, the axisymmetric part. All non-axisymmetric components of deformation are assumed to be inextensible. This assumption greatly simplifies the analysis by allowing the circumferential displacements v to be described in terms of the radial displacements w. This condition of inextensionality can be expressed as:

$$W - \frac{\partial V}{\partial \theta} \approx W_o \tag{21}$$

Physically, this approximation assumes that, to first order in displacements, flexure of the tube produces no net change in length of the tube's middle surface. This aspect of the model is similar to the inextensional static buckling model described by Timoshenko and Gere (1961), with the exception that they assumed the motion to be completely inextensional, i.e., $W_o = 0$. The inextensional approximation typically improves as the tube is made thinner or the wavelength of flexural motion grows

longer (i.e., for low mode numbers n). In terms of the Fourier coefficients of (20), the inextensional condition implies that $nV_n = W_n$, $n\beta_n = \delta_n$, and $n\alpha_n = -\gamma_n$.

Using the inextensional model, Lindberg and Florence (1987) showed that the integrals for the strain energy and kinetic energy given in (19) evaluate to:

$$T_K = \frac{Eha\pi}{(1-\nu^2)}\left\{\dot{W}_o^2 + \frac{1}{2}\sum_{n=2}^{\infty}\left(\frac{n^2+1}{n^2}\right)\dot{W}_n^2\right\} \tag{22}$$

$$U = \frac{Eha\pi}{(1-\nu^2)}\left\{W_o^2 + \frac{1}{2}\sum_{n=2}^{\infty}\left[\beta^2(n^2-1)^2 - W_o(n^2-2)\right]W_n^2 - \sum_{n=2}^{\infty} W_o(n^2-2)\delta_n W_n\right\} + O(W_n^4) \tag{23}$$

In calculating these integrals, many of the terms involved in the strain-displacement equations integrate identically to zero due to the orthogonality of the trigonometric functions. Because of this property, only one of the Fourier coefficients for the shape imperfections, namely δ_n, plays a role in the response. A number of 4^{th} order terms arising in (23) have been listed as $O(W_n^4)$, and will be excluded from the subsequent analysis since they are small during the initial stages of buckling.

The integral (19c) for the pressure work can be expressed as:

$$W_p = \frac{Eha}{(1-\nu^2)}\int_0^{2\pi}\left[P_o W_o + \sum_{n=2}^{\infty}\left[P_o W_n\cos(n\theta) + W_o P_n\cos(n\theta)\right] + \sum_{n=2}^{\infty}\sum_{m=2}^{\infty} P_n W_m\cos(n\theta)\cos(m\theta)\right]d\theta \tag{24}$$

The first-order terms integrate to zero and the second order terms are nonzero only if $m = n$, due to the orthogonality of the cosines. The resulting expression for the pressure work is:

$$W_p = \frac{Eha\pi}{(1-\nu^2)}\left[2P_o W_o + \sum_{n=2}^{\infty} P_n W_n\right] \tag{25}$$

Having obtained expressions for the kinetic energy, strain energy, and work due to external loads, ordinary differential equations for the Fourier modes W_o and W_n can now be obtained from Lagrange's equation of motion:

$$\frac{d}{dT}\left(\frac{\partial T_K}{\partial \dot{q}_i}\right) - \frac{\partial T_K}{\partial q_i} + \frac{\partial U}{\partial q_i} = \frac{\partial W_p}{\partial q_i} \tag{26}$$

where q_i is a generalized displacement, which may be either W_o or W_n. The respective equations of motion for $q_i = W_o$ and $q_i = W_n$ are the following:

$$\ddot{W}_o + W_o = P_o + O(W_n^2) \tag{27a}$$

$$\left(\frac{n^2+1}{n^2}\right)\ddot{W}_n + \left[\beta^2(n^2-1)^2 - W_o(n^2-2)\right]W_n = P_n + W_o(n^2-2)\delta_n + O(W_n^3) \tag{27b}$$

The first equation (27a) describes the axisymmetric component of the deformation. As shown, this equation contains a term which is quadratic in W_n so that (27a) and (27b) are coupled. Goodier and McIvor (1964) have considered retaining this non-linear coupling and predicted a cyclic transfer of energy between the axisymmetric vibrations W_o and non-axisymmetric vibrations W_n. However, in our experiments we have observed that the small amplitude and rapid damping of axisymmetric vibrations preclude autoparametric excitation of this sort, and hence the nonlinear terms are neglected.

The second equation (27b) describes the growth of non-axisymmetric Fourier modes W_n, the motion of which is forced by W_o. This equation also contains nonlinear terms of cubic order which couple the motion amongst the non-axisymmetric modes (Lindberg and Florence, 1987). However, this coupling can be neglected on the grounds that cubic terms are small during the initial stages of buckling, an assumption which is supported by our experiments which show no evidence of coupling between modes.

To solve (27), one requires a model for the shape imperfection δ_n. The shape imperfection can sometimes be measured, although this is difficult for small imperfections or large mode numbers n. A common alternative is to assume shape imperfections of unit amplitude and analyze the amplification of buckles, that is, their growth relative to the size of the shape imperfection (Lindberg and Florence, 1987). Another technique is to choose random imperfections that satisfy an appropriate statistical distribution (Lindberg, 1988).

In our experiments, we have found that wall thickness variations are the dominant imperfection rather than shape imperfections. Whereas shape imperfections describe an initial non-circularity of the tube in the absence of applied loads, wall thickness variations are characterized by a circumferentially-varying wall thickness that is present in a perfectly circular tube. In practice, both types of imperfections are always present.

3.2.1 Self-induced Pressure Loads

In (27b), the parameter P_n is the acoustic pressure load due to vibration of the tube and resonance in the surrounding annulus of water. To model P_n, the fluid motion is described using the linear wave equation for the velocity potential ϕ:

$$\frac{1}{c^2}\frac{\partial^2\phi}{\partial t^2} = \frac{\partial^2\phi}{\partial r^2} + \frac{1}{r}\frac{\partial\phi}{\partial r} + \frac{1}{r^2}\frac{\partial^2\phi}{\partial\theta^2} \tag{28}$$

If the velocity potential is represented using a Fourier series expansion in θ and harmonic vibrations are assumed with frequency ω, then (28) reduces to a Helmholtz equation for each Fourier mode ϕ_n:

$$r^2\frac{\partial^2\phi_n}{\partial r^2}+r\frac{\partial\phi_n}{\partial r}+\left(\frac{r^2\omega^2}{c^2}-n^2\right)\phi_n=0 \tag{29}$$

In general the solutions to this equation are either Bessel functions (for a bounded domain, such as an annulus) or Hankel functions (for an unbounded domain). However, in many situations the frequency of vibration is low enough that an incompressible approximation is applicable. Referring to (29), the criterion for which this approximation can be made is:

$$\frac{r^2\omega^2}{c^2n^2}<<1 \tag{30}$$

In our current experiments, this quantity is less than about 0.01, so the frequency term in (29) can be neglected. A physical interpretation of this approximation is that the reverberation time of pressure waves is much shorter than the period of structural vibration, so the radiated pressure field can be treated as uniform. This is also equivalent to taking the limit of $c\to\infty$ in (28), such that the fluid is incompressible. After applying this low-frequency approximation, (29) reduces to a Cauchy-Euler equation:

$$r^2\frac{\partial^2\phi_n}{\partial r^2}+r\frac{\partial\phi_n}{\partial r}-n^2\phi_n=0 \tag{31}$$

which has solutions $r^{\pm n}$. The relevant boundary conditions at the rigid outer wall $(r=b)$ and the deforming inner wall $(r=a)$ are that the radial fluid velocity must match the radial speed of the wall:

$$\left.\frac{\partial\phi}{\partial r}\right|_{r=b}=0 \qquad\qquad \left.\frac{\partial\phi}{\partial r}\right|_{r=a}=-\frac{\partial w_n}{\partial t} \tag{32}$$

The minus sign in the second boundary condition is needed because the tube displacement is defined positive inward. Applying these boundary conditions, the solution for the velocity potential is:

$$\phi_n(r,t)=\frac{\partial w_n}{\partial t}\frac{a}{n}a^nb^n\left[\frac{(r/b)^n+(b/r)^n}{b^{2n}-a^{2n}}\right] \tag{33}$$

Within the linear theory used to model the fluid (Lighthill, 1978), pressure is related to the velocity potential by:

$$p=-\rho_w\frac{\partial\phi}{\partial t} \tag{34}$$

As a result, the pressure at the tube wall $(r=a)$ is found to be:

$$-p_n = \left[\frac{\rho_w a}{n}\left(\frac{(b/a)^{2n}+1}{(b/a)^{2n}-1}\right)\right]\frac{\partial^2 w_n}{\partial t^2} \equiv m\frac{\partial^2 w_n}{\partial t^2} \tag{35}$$

The constants which pre-multiply the tube acceleration $\ddot{w}_n$ have been labeled m since they describe the effective added mass of the fluid. Since the self-induced pressure p_n contains only terms proportional to $\ddot{w}_n$, the effect of the liquid is purely mass-like and contributes only to a change in vibration frequency with no damping. Such behavior is characteristic of incompressible fluid models; however, the same purely mass-like behavior is observed even when the exact solution to (29) is used instead of the incompressible approximation. To obtain this exact solution, one would express solutions to (29) in terms of Bessel functions and solve the eigenvalue problem which arises when boundary conditions (32) are applied. To each of the resulting eigenfrequencies there corresponds a purely mass-like contribution to the pressure. This property is a consequence of the confined, annular geometry for which no energy-radiation mechanism is present. In contrast, when a tube is submerged in an unbounded medium, the fluid-structure interaction produces terms that are both mass-like (proportional to $\ddot{w}$) and resistive (proportional to $\dot{w}$) which results in damping of vibrations (Junger and Feit, 1972).

After the self-induced pressure of (35) has been made dimensionless using (18), it is applied to the equations of motion (27). It is convenient also to define a dimensionless added mass coefficient M as follows:

$$M \equiv \frac{m}{\rho h}\frac{n^2}{n^2+1} = \left[\frac{\rho_w a}{\rho h n}\left(\frac{(b/a)^{2n}+1}{(b/a)^{2n}-1}\right)\right]\left(\frac{n^2}{n^2+1}\right) \tag{36}$$

Using this definition of the added mass coefficient, (27) can be re-written:

$$\ddot{W}_o + W_o = P_o \tag{37a}$$

$$\ddot{W}_n + \left[\Omega_n^2 - F_n^2 W_o(T)\right] W_n = F_n^2 W_o(T)\delta_n \tag{37b}$$

where

$$\Omega_n^2 = \frac{n^2\beta^2(n^2-1)^2}{(1+M)(n^2+1)} \tag{38}$$

$$F_n^2 = \frac{n^2(n^2-2)}{(1+M)(n^2+1)} \tag{39}$$

The parameter Ω_n is the frequency of free vibration for mode number n, while the parameter F_n models the interaction between the axisymmetric mode W_o and the nonsymmetric modes W_n.

Verification of this model was obtained by comparing the natural frequency predictions of (38) with some experimental measurements, as shown in Table 1. Experimental values were found using the same setup that was used to examine buckling; in this setup we can also measure the long-time frequencies of elastic vibration which occur when tubes are subjected to loads near, but not above, the buckling

Table 1 Comparison of measured and predicted natural frequencies. "No FSI" indicates frequencies calculated using (38) with $M = 0$, while values in the column labeled "FSI" were computed with the values of M listed in the table. The percent error is computed between the measured frequencies and the frequencies calculated with the inclusion of FSI.

Material	a/h	h [mm]	n	M	— Frequency [kHz] —			Error
					No FSI	FSI	Measured	[%]
6061 Alum.	13.5	1.47	2	2.3	2.45	1.35	1.36	1.0
6061 Alum.	17.4	0.89	2	2.7	2.46	1.28	1.21	5.6
6061 Alum.	17.4	0.89	2	2.7	2.46	1.28	1.20	6.5
6061 Alum.	17.4	0.89	2	2.7	2.46	1.28	1.24	3.1
6061 Alum.	17.4	1.24	2	3.2	1.76	0.86	0.85	1.4
304 SS	17.4	0.89	2	0.9	2.36	1.70	1.82	6.3
6061 Alum.	24.5	0.89	2	4.5	1.24	0.53	0.54	2.4
6061 Alum.	17.4	1.24	3	2.1	4.98	2.84	2.82	0.9
6061 Alum.	17.4	0.89	3	2.0	6.97	4.06	3.97	2.3
6061 Alum.	24.5	0.89	3	2.9	3.50	1.77	1.85	4.5

threshold (see, for example, Fig. 6). Frequencies were extracted from the strain traces either by using fast fourier transforms or by counting periods, depending on how many cycles were present in the data. Only mode numbers 2 and 3 are included in Table 1 since only these modes were observed in experiment. In some cases (such as Fig. 7), vibration frequencies from more than one mode could be extracted from a single strain trace.

The results in Table 1 demonstrate fair agreement between the predicted and measured frequencies. This validates a number of assumptions involved in the model, including the 2D plane strain approximation, the neglect of axial bending, and the incompressible FSI model. Good agreement with the experiments was still found even for vibrations of large amplitude approaching yielding of the tube, which suggests that the shell model described above is reasonable over the whole range of elastic deformations that we seek to model. This result also confirms that our neglect of geometrical nonlinearities (quadratic and cubic terms in the shell equations (27)) is reasonable.

3.2.2 Static Buckling

Before considering dynamical solutions to (37), it is interesting to explore the static buckling limit of this equation. Taking the time derivatives equal to zero, we find that $W_o = P_o$ and displacements W_n become unbounded when $\Omega_n^2 = F_n^2 P_o$. This criterion yields the static buckling pressure for the n^{th} mode:

$$P_{crn} = \beta^2 \frac{(n^2-1)^2}{n^2-2} \tag{40}$$

When written in terms of dimensional variables, the static buckling limit becomes

$$p_{crn} = \frac{Eh^3}{12(1-\nu^2)a^3}\frac{(n^2-1)^2}{n^2-2} \tag{41}$$

This result differs slightly from the classical static buckling threshold for an infinitely long tube derived by Timoshenko and Gere (1961):

$$p_{crn} = \frac{Eh^3}{12(1-\nu^2)a^3}(n^2-1) \tag{42}$$

The discrepancy arises primarily because in the development of (27), the pressure force was taken in the direction of the undeformed normal rather than that of the deformed normal. This problem has been encountered in other shell formulations, as evaluated by Simitses and Aswani (1974). This difference is smaller for larger values of n; for $n \geq 5$, the error is less than 5%.

3.2.3 Direct integration of Fourier Modes

For a general pressure load $P_o(T)$, (37) cannot be solved analytically. However, numerical solutions to this pair of uncoupled ordinary differential equations can be easily integrated with modern computational tools. To demonstrate the predictions of this model, experimentally measured pressure traces were fed into the model as P_o and the numerical solution was computed for the first 10 Fourier modes. To make comparisons with experimental measurements, it was necessary to estimate the numerical value of the shape imperfections δ_n in (37). This was done by multiplying the measured variations in wall thickness (described in Sec. 2) by a factor of a/h, an approach which was motivated by comparing the relative contributions of shape imperfections and wall thickness variations to the total strain energy of the tube.

After solving for the dimensionless displacements W_o and W_n, hoop strains at the outer surface of the tube were calculated using (14) and (15). Strains were evaluated at angles of 0°, 90°, and 180° around the circumference, which is where the corresponding strain gauges from experiment were located. The results are compared with the experimental strain measurements in Fig. 14.

Both the simulation and the experiment feature a superposition of vibrations of modes 2 and 3. The amplitude and frequency of both modes is well-predicted, with the exception that the numerical solution does not predict any damping. This behavior is a consequence of the incompressible fluid model and the omission of mechanical damping within the tube material.

The membrane strain from the experiments was estimated by averaging the measurements from two strain gauges located 90°apart. Since these guages were located on the major and minor axes of the vibration, averaging their measurements cancels out any bending strain due to mode 2 vibration (though bending strains from modes 3 and higher are not necessarily canceled). Good agreement between the measured and simulated membrane strains is also observed. These results demonstrate that in spite of the numerous simplifications used to develop this buckling model, the predictions are in remarkably good agreement with experimental measurements.

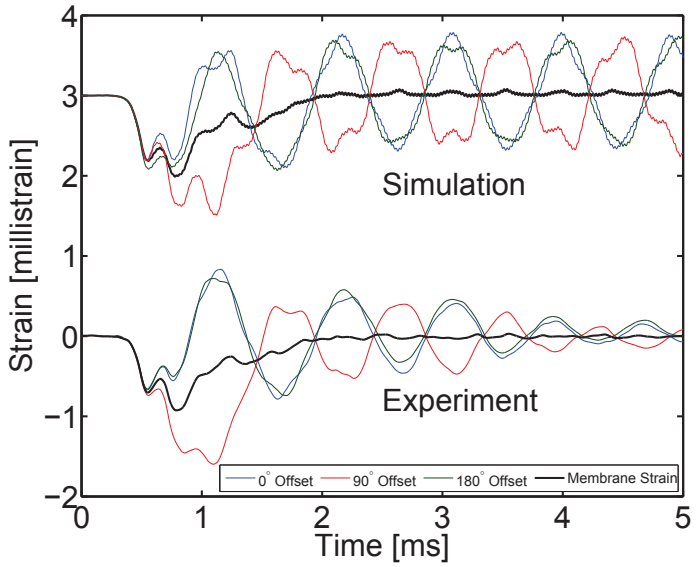

Fig. 14 Comparison of simulations and experiments for a steel tube very near the buckling threshold. Traces have been offset for clarity. Tube is 304 stainless steel with radius $a = 22$ mm and $a/h = 17.4$.

3.2.4 Generalized Loads

Although integrating the dynamic response of a tube for a given pressure load is often of interest, in many cases it is preferable to study the response to a class of generalized dynamic loads rather than to a specific load. Several types of loads that are of practical interest are a square wave of finite duration, a triangular wave, and an exponentially decaying wave. These pulse shapes can be used as idealized representations of many practical loads, such as shock or blast waves. Each of these pulse shapes can be characterized by a peak pressure P_i and a total impulse I, which is the integral of the pressure distribution over time. It is also convenient to define a characteristic load duration, $\tau \equiv I/P_i$.

In Sec. 2.1 it was observed experimentally that prior to buckling, the strain consists of small vibrations around the quasi-static value. Since these vibrations are small and damp out quickly, it is reasonable to neglect the axisymmetric breathing motion altogether and assume that the hoop strain consists only of its quasi-static component. In terms of the present non-dimensional variables, this means that $W_o \approx P_o$.

It should be recognized that neglecting the dynamics of axisymmetric vibration eliminates the possibility of autoparametric excitation. Such excitation has been the subject of much research (Goodier and McIvor, 1964, Lindberg, 1964, 1974), but is usually not observed in experiments due to the internal damping that is present in real materials. Lindberg (1974) considered this problem in detail and found that

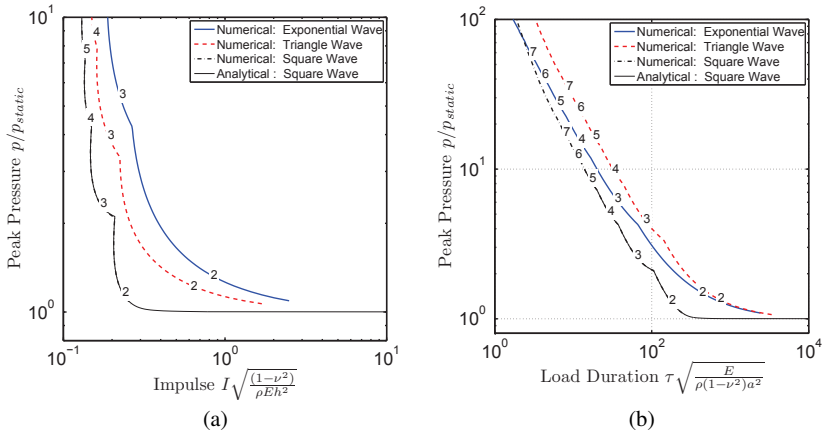

Fig. 15 a) Buckling threshold in terms of pressure and impulse. b) Buckling threshold in terms of pressure and load duration. Numbers indicate the most unstable mode number n_{cr}. Curves were computed with a/h=20 and an amplification of 100.

since autoparametric buckling often occurs only after a large number of vibration cycles, it is mitigated by even small amounts of damping. As a result, he was able to observe experimental evidence of autoparametric buckling only under very carefully chosen test conditions. In our present experiments, the small amplitude and fast damping of axisymmetric vibrations due to FSI add further evidence that for submerged structures, autoparametric excitation is likely to be insignificant and axisymmetric vibrations can be neglected. Disregarding the axisymmetric vibration is also appropriate only if the load duration is longer than the period of these vibration, which is the case here.

To study the buckling of tubes under square, triangular, and exponential loads, it is necessary to choose a criterion for the buckling threshold. A convenient choice is to consider the tube to be buckled when the maximum displacement divided by the initial shape imperfection exceeds a particular amplification, A. The buckling threshold can then be determined by choosing a peak pressure P_i and integrating (37) numerically, gradually increasing the load duration τ until one of the Fourier modes exceeds the chosen amplification A. This value of τ then marks a point on the buckling threshold. By repeating this process for many values of P_i, the buckling threshold can be mapped out. This same approach was taken by Lindberg and Florence (1987), who investigated the effects of pulse shape and amplification A on the computed buckling threshold and concluded that both effects are small.

Examples of buckling thresholds for $a/h = 20$ obtained using this method are plotted in Fig. 15. An amplification of $A = 100$ was chosen, so these curves represent contours along which the maximum deformation is 100 times the size of the initial imperfection. The numbers along the curves indicate the most unstable mode number. Although the amplification value of A = 100 has been arbitrarily chosen, it

is representative of realistic values and the qualitative features of the results are not sensitive to the precise value of A.

In Fig. 15a, the buckling threshold is plotted in terms of the dimensionless pressure and impulse. This plot reveals that the buckling threshold tends towards two asymptotes: there are a minimum pressure (the static buckling pressure) and a minimum impulse below which the tube is always stable. The differences between the three load shapes are quite small along these asymptotes, but near the knee in the curve larger differences are observed. As will be seen, this is the region in which our experimental measurements were recorded.

In Fig. 15b, the same buckling threshold data is represented on a plot of peak pressure vs. dimensionless load duration τ. In this scaling, the period of axisymmetric vibration falls at 2π on this plot, which is far below the knee in the curve. This reveals that the dynamic buckling pressure can be more than an order of magnitude greater than the static buckling pressure even for loads that are classified as "quasi-static".

3.3 Effects of FSI

Recall from the fluid-structure interaction model developed in Section 3.2.1 that the dimensionless added mass of the fluid is given by:

$$M = \frac{1}{n}\frac{\rho_w}{\rho}\frac{a}{h}\left[\frac{(b/a)^{2n}+1}{(b/a)^{2n}-1}\right]\left(\frac{n^2}{n^2+1}\right) \tag{43}$$

For a tube submerged in an infinite medium, the term in brackets tends to 1 and the added mass depends only on the ratio of densities, the thickness of the tube, and the mode number. Since the added mass is always greater for lower mode numbers, this indicates that FSI effects are most pronounced near the knee in the buckling threshold curve, where the mode numbers are smallest.

Examples of buckling threshold curves are plotted in Fig. 16 for tubes made from several practical materials and submerged in air and water. The tubes are subjected to a square-wave pressure pulse, and the amplification chosen to define the buckling threshold is $A = 100$. As expected, the effect of the fluid is greatest near the knee in the curve, and is largest for tubes of low density[1]. For comparison with our experiments, the buckling thresholds in Fig. 16 were computed for relatively thick tubes, with $a/h = 20$. Under these conditions, the added mass coefficient for an aluminum tube with $n = 2$ is about $M = 3$ and the buckling threshold is shifted to the right by about a factor of $\sqrt{1+M} = 2$. However, for very thin shells ($a/h \sim 100$) and lightweight materials, or for tubes in a confined space, the added mass coefficient can be on the order of 30-40 and can shift the buckling threshold by a factor as high as 5-7.

[1] For composite materials, the non-isotropic stiffness can affect the buckling behavior in other ways, but the added mass effect is expected to follow the same scaling as for metal tubes.

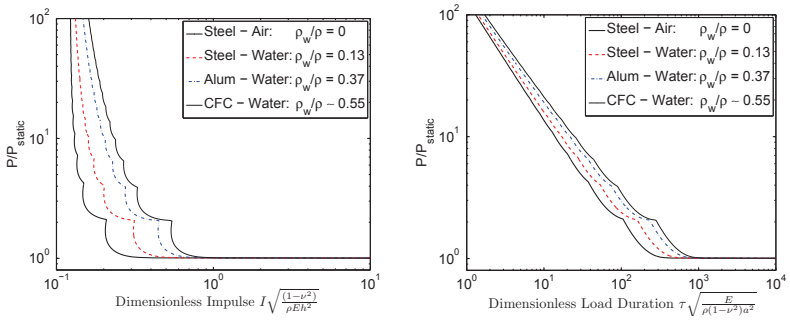

Fig. 16 Effect of added mass on buckling threshold for a square-wave pressure pulse with $a/h = 20$ and several tube materials. CFC is carbon fiber composite. a) Bucking threshold in terms of pressure and impulse. b) Buckling threshold in terms of pressure and load duration.

Because of the primarily mass-like influence of FSI, the only effect of the fluid is to decrease the frequency of vibrations or the growth rate of buckles. In fact, by re-scaling the time variable T in (37b) by a factor of $\sqrt{1+M}$, one can eliminate the added mass from the equation entirely. This would suggest that if one computes the buckling threshold for a tube *in vacuo*, then the corresponding threshold curve for a submerged tube can be obtained by re-scaling the load duration τ by a factor of $\sqrt{1+M}$. Since M is a function of mode number, this re-scaling would have to be done separately for each segment of the buckling threshold.

A nuance to this approach is that the presence of FSI shifts the transition points at which the most unstable mode number changes from one to the next. However, as shown in Fig. 16, the transition points do not shift very much. This suggests that the naïve approach of simply shifting the *in vacuo* buckling threshold to the right by a factor of $\sqrt{1+M}$ will still provide reasonable predictions. In fact, this has been done for the tube shown in Fig. 16, and the results (not shown) were nearly indistinguishable from the curves plotted in the figure.

3.4 Comparison with Experiments

Having developed a theoretical model for the buckling of cylindrical tubes, we now consider how well its predictions compare with experimental measurements. This comparison is made in Fig. 17 for aluminum tubes with $a/h = 17.4$ and 24.5. For each tube size, the data is represented using both the impulse and the load duration as independent variables. The theoretical curves were computed by assuming an exponential load shape and an amplification of $A = 100$, while experimental data points correspond to the conditions at which plastic deformation was first observed. Good agreement between the experiments and predictions is observed.

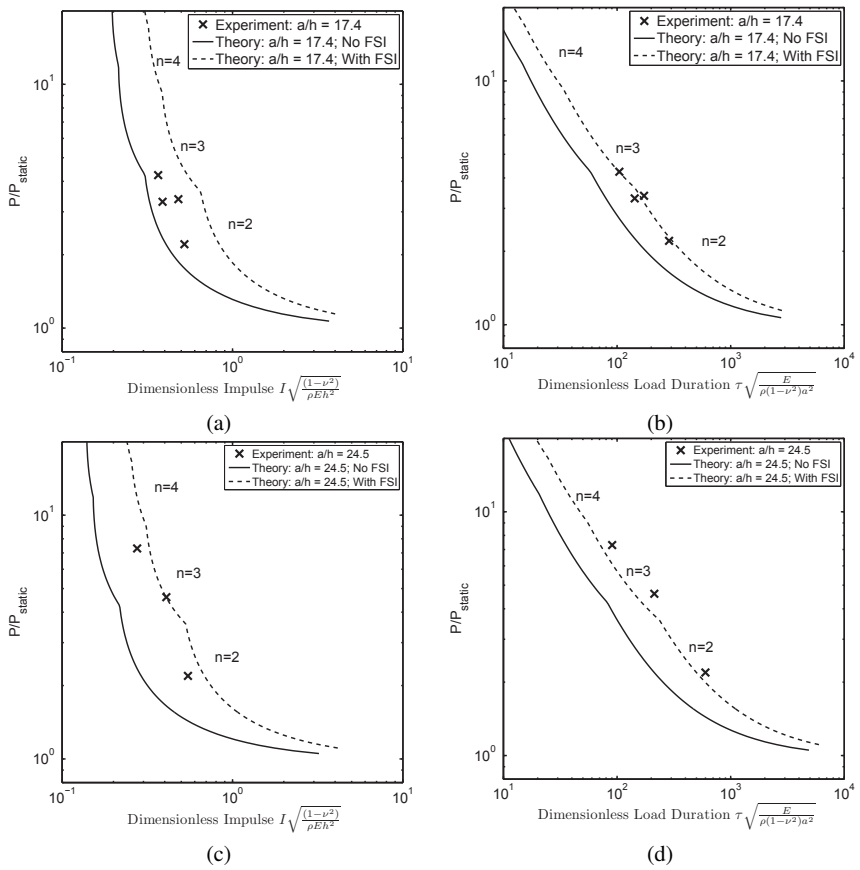

Fig. 17 Comparison of predicted and experimental buckling thresholds 6061-T6 aluminum tubes. Theoretical predictions are computed assuming an exponential pulse shape and an amplification of $A = 100$. **a)** Buckling threshold for $a/h = 17.4$ in terms of load impulse. **b)** Same as a), but in terms of load duration. **c)** Buckling threshold for $a/h = 24.5$ in terms of load impulse. **d)** Same as c), but in terms of load duration.

For each value of a/h, Fig. 17 includes buckling thresholds both with and without the effects of fluid-structure interaction. In most cases, the experimental data points lie closer to the curve for which the effects of FSI are included. However, since the tubes are fairly thick, the effects of fluid-structure interaction are rather small and demonstration of the added mass effect based on these results is by no means conclusive.

A final observation from Fig. 17 is that some data points lie near the boundary at which the most unstable mode transitions from 2 to 3. Such behavior was confirmed in the experiments: tubes subjected to loads near this boundary exhibited excitation of both modes 2 and 3. However, the theoretical curves were computed by assuming

that each mode is excited independently, whereas in the experiments tube failure occurred via a superposition of multiple excited modes (see, for instance, Fig. 7). This demonstrates that the most excited mode does not transition abruptly, but rather a gradual transition is made over a range of pressures and impulses in which two or more modes are strongly excited.

4 Summary

This chapter has considered the dynamic buckling of tubes with an emphasis on the complexities that arise when the tubes are submerged in a dense fluid. Experimental measurements of dynamic strains have clarified the behavior of the tube during the intermediate stages of buckling, a subject which has not been studied in detail in the literature. These results have confirmed many of the theoretical expectations that have been developed in the past, including the shape of the buckling threshold on a pressure-impulse diagram and the increase in the most unstable mode number as the applied pressure is increased. The experiments have also demonstrated that variations in wall thickness around the circumference of the tube have a significant and repeatable effect on the orientation of the tube's vibration and buckling which is in good agreement with theoretical predictions.

The experimental measurements have also clarified several of the effects of fluid-structure interaction on the dynamic response of the tubes. Measured vibration frequencies were in good agreement with theoretical added-mass models, and an incompressible fluid model was found to capture the added-mass effects quite adequately due to the relatively low frequency of non-axisymmetric vibrations. Due to FSI, axisymmetric vibrations were found to play only a small role in the response of the tube and measured hoop strains were quite close to those predicted by static models. The coupling between non-axisymmetric motion and the fluid pressure was found to be small due to the negligible volume changes involved in these vibrations; however, at the onset of plastic deformation, these volume changes were no longer negligible.

A two-dimensional buckling model was developed by making approximations based on the observations from experiments, and good agreement with both dynamic strain measurements and buckling threshold measurements was obtained. This model showed that the main effect of FSI is a reduction in the growth rate of buckles; depending on the extent of the fluid-structure interaction, this reduced growth rate can increase the impulse the tube can withstand by a factor as high as 5-7.

Acknowledgements Much of the work presented in this chapter was supported by the Office of Naval Research DOD MURI on Mechanics and Mechanisms of Impulse Loading, Damage and Failure of Marine Structures and Materials (ONR Grant No. N00014-06-1-0730), under program manager Dr. Y. D. S. Rajapakse. Mr. Tomohiro Nishiyama, currently at the Japan Patent Office, and Prof. Kazuaki Inaba, currently at the Tokyo Institute of Technology, executed the initial design and supervised the fabrication of the annular tube implosion fixture while working at Caltech. Mr. Ja-

son Damazo and Dr. Rafal Porowski, currently at the research Center for Fire Protection in Poland, carried out preliminary experiments on buckling using the initial fixture design. Prof. Ravichandran of Caltech provided essential technical advice and encouragment as well as leadership of the Caltech MURI .

References

G.R. Abrahamson and J.N. Goodier. Dynamic plastic flow buckling of a cylindrical shell from uniform radial impulse. In *Proceedings of the Fourth National Congress of Applied Mechanics*, volume 2, pages 939–950, 1962.

G.R. Abrahamson, A.L. Florence, and H.E. Lindberg. Investigation of response of simplified ICBM-type structures to impulsive loading. Technical Report AFWL-TR-65-136, Stanford Research Institute, 1966.

D.L. Anderson and H.E. Lindberg. Dynamic pulse buckling of cylindrical shells under transient lateral pressures. *AIAA Journal*, 6(4):589–598, 1968.

S.B. Batdorf. A simplified method of elastic-stability analysis for thin cylindrical shells. Technical Report TR 847, NACA, 1947.

W. Beltman and J.E. Shepherd. Linear elastic response of tubes to internal detonation loading. *Journal of Sound and Vibration*, 252(4), 2002.

B. Budiansky and J.W. Hutchinson. Dynamic buckling of imperfection-sensitive structures. In H. Gortler, editor, *Proceedings of the Eleventh International Congress of Applied Mechanics*, pages 636–651. Springer-Verlag, 1965.

S. Chonan. Response of fluid-filled cylindrical shell to a moving load. *Journal of Sound and Vibration*, 55(3):419–430, 1977.

J.S. Damazo, R. Porowski, J.E. Shepherd, and K. Inaba. Fluid-structure interaction of submerged tubes subjected to impact generated stress waves. In *Proceedings of the 16th US National Congress of Theoretical and Applied Mechanics*. ASME, 2010. USNCTAM2010-1279, June 27-July 2, 2010, State College, Pennsylvania, USA.

G.D. Galletly and R. Bart. Effects of boundary conditions and initial out-of-roundness on the strength of thin-walled cylinders subject to external hydrostatic pressure. *Journal of Applied Mechanics*, 23:351–358, 1956.

J.N. Goodier and I.K. McIvor. The elastic cylindrical shell under nearly uniform radial impulse. *Journal of Applied Mechanics*, 31:259–266, 1964.

G.A. Hegemier. Instability of cylindrical shells subjected to axisymmetric moving loads. *Journal of Applied Mechanics*, 33(2):289–296, 1966.

G.A. Hegemier. Stability of cylindrical shells under moving loads by the direct method of Liapunov. *Journal of Applied Mechanics*, 34:991–998, 1967.

J.W. Hutchinson and B. Budiansky. Dynamic buckling estimates. *AIAA Journal*, 4 (2):525–530, 1966.

J.W. Hutchinson and W.T. Koiter. Postbuckling theory. *Applied Mechanics Reviews*, 23(12):1353–1366, 1970.

Kazuaki Inaba and Joseph E. Shepherd. Flexural waves in fluid-filled tubes subject to axial impact. *J. Pressure Vessel Technol.*, 132:021302, April 2010.

J.P. Jones and P.G. Bhuta. Response of cylindrical shells to moving loads. *Journal of Applied Mechanics*, 31(1):105–111, 1964.

N. Joukowsky. Über den hydraulishen stoss in wasserleitungsröhren (on the hydraulic hammer in water supply pipes). *Mémoires de l'Académie Impériale des Sciences de St. Péterbourg*, 9(5), 1900. Series 8.

Miguel C. Junger and David Feit. *Sound, Structures, and their Interaction*. MIT Press, second edition, 1972.

J. Kempner, K.A. Pandalai, S.A. Patel, and J. Crouzet-Pascal. Postbuckling behavior of circular cylindrical shells under hydrostatic pressure. *Journal of the Aeronautical Sciences*, 24:253–264, 1957.

W.T. Koiter. *On the Stability of Elastic Equilibrium*. PhD thesis, Polytechnic Institute Delft, 1945.

D. Korteweg. Über die fortphlanzungsgeschwindigkeit des schalles in elastisches röhren (on the velocity of propagation of sound in elastic pipes). *Annalen der Physik und Chemie*, 9(5):525–542, 1878.

Arthur W. Leissa. Vibration of shells. Technical Report NASA SP-288, National Aeronautics and Space Administration, 1973.

James Lighthill. *Waves in Fluids*. Cambridge University Press, 1978.

C.T. Lin and C.W. Morgan. A study of axisymmetric vibrations of cylindrical shells as affected by rotatory inertia and transverse shear. *Journal of Applied Mechanics*, 23(2), 1956.

H. E. Lindberg and R. D. Firth. Structural response of spine vehicles, volume II: Simulation of transient surface loads by explosive blast waves. Technical Report AFWL-TR-66-163, Vol. II, Stanford Research Institute, 1967.

H.E. Lindberg. Random imperfections for dynamic pulse buckling. *Journal of Engineering Mechanics*, 114(7):1144–1165, 1988.

H.E. Lindberg and A.L. Florence. *Dynamic Pulse Buckling*. Martinus Nijhoff Publishers, 1987.

H.E. Lindberg, D.L. Anderson, R.D. Firth, and L.V. Parker. Response of reentry vehicle-type shells to blast loads. Technical Report LMSC-B130200-VOL-4-C, Stanford Research Institute, 1965.

Herbert E. Lindberg. Buckling of a very thin cylindrical shell due to an impulsive pressure. *Journal of Applied Mechanics*, 31:267–272, 1964.

Herbert E. Lindberg. Stress amplification in a ring caused by dynamic instability. *Journal of Applied Mechanics*, 41:392–400, 1974.

Herbert E. Lindberg and George E. Sliter. Response of reentry-vehicle-type shells to transient surface pressures. Technical Report AFWL-TR-68-56, Stanford Research Institute, 1969.

D. Lockhart and J.C. Amigazo. Dynamic buckling of externally pressurized imperfect cylindrical shells. *Journal of Applied Mechanics*, 42:316–320, 1975.

P. Mann-Nachbar. On the role of bending in the dynamic response of thin shells to moving discontinuous loads. *Journal of the Aerospace Sciences*, 29:648–657, 1962.

I.K. McIvor and E.G. Lovell. Dynamic response of finite length cylindrical shells to nearly uniform radial impulse. *AIAA Paper*, (No. 68-144), 1968.

N.W. McLachlan. *Theory and Application of Mathieu Functions*. Dover Publications Inc., first edition, 1964.

Kh.M. Mushtari and K.Z. Galimov. Nonlinear theory of thin elastic shells. Technical Report NASA-TT-F62, 1961. Translated from Tatknigoizdat, Kazan' 1957.

P.M. Naghdi and R.M. Cooper. Propagation of elastic waves in cylindrical shells, including effects of transverse shear and rotary inertia. *Journal of the Acoustical Society of America*, 28(1):56–63, 1956.

K. Schiffner and C. R. Steele. Cylindrical shell with an axisymmetric moving load. *AIAA Journal*, 9(1):37–47, 1971.

J. E. Shepherd and K. Inaba. Shock loading and failure of fluid-filled tubular structures. In A. Shukla, G. Ravichandran, and Y. Rajapakse, editors, *Dynamic Failure of Materials and Structures*, pages 153–190. Springer, 2010.

J.E. Shepherd. Structural response of piping to internal gas detonation. *Journal of Pressure Vessel Technology*, 131(3):031204, 2009.

George J. Simitses. Buckling and postbuckling of imperfect cylindrical shells: A review. *Applied Mechanics Reviews*, 39(10), 1986.

G.J. Simitses and M. Aswani. Buckling of thin cylinders under uniform lateral loading. *Journal of Applied Mechanics*, 41(3):827–829, 1974.

T.E. Simkins, G.A. Pflegl, and E.G. Stilson. Dynamic strains in a 60 mm gun tube: An experimental study. *Journal of Sound and Vibration*, 168(3):549–557, 1993.

L.H. Sobel. Effects of boundary conditions on the stability of cylinders subject to lateral and axial pressures. *AIAA Journal*, 2(8):1437–1440, 1964.

M. Stein. The influence of prebuckling deformations and stresses on the buckling of perfect cylinders. Technical Report TR R-190, NASA, 1964.

Sing-chih Tang. Dynamic response of a tube under moving pressure. In *Proceedings of the American Society of Civil Engineers. Engineering Mechanics Division. Volume 5*, pages 97–122, 1965.

J.G. Teng. Buckling of thin shells: Recent advances and trends. *Applied Mechanics Reviews*, 49(4):263–274, 1996.

A.S. Tijsseling. Fluid-structure interactions in liquid-filled pipe systems: A review. *Journal of Fluids and Structures*, 10:109–146, 1996.

S. P. Timoshenko and J. M. Gere. *Theory of Elastic Stability*. McGraw-Hill, 2nd edition, 1961.

David C. Wiggert and Arris S. Tijsseling. Fluid transients and fluid-structure interaction in flexible liquid-filled piping. *Applied Mechanics Reviews*, 54(5):455–481, 2001.

E. Benjamin Wylie and Victor L. Streeter. *Fluid Transients in Systems*. Prentice Hall, 1993.

N. Yamaki. Influence of prebuckling deformations on the buckling of circular cylindrical shells under external pressure. *AIAA Journal*, 7(4):753–755, 1969.

N. Yamaki. *Elastic Stability of Circular Cylindrical Shells*. Elsevier Science Publishing Co., 1984.